This article has been accepted for publication in a future issue of this journal, but has not been fully edited. Content may change prior to final publication. Citation information: DOI 10.1109/TIE.2019.2952829, IEEE Transactions on Industrial Electronics

Flux-controlled Hybrid Reluctance Actuator for High-precision Scanning Motion

Shingo Ito, Francesco Cigarini, and Georg Schitter, *Senior Membership*

***Abstract*—To achieve highly precise and linear scanning motion by a hybrid reluctance actuator (HRA), this paper proposes a flux-controlled mode that uses regulated magnetic flux as the control input for the actuator operation and evaluates its performance in comparison with the conventional current-controlled mode. In the conventional case, HRAs exhibit magnetic nonlinearities (e.g. hysteresis) and position-dependent force that can make the system unstable. A model-based analysis reveals that they are included in the variable magnetic flux of a HRA. Thus, they are captured by flux estimation and rejected by flux feedback control for high quality scanning motion. For the estimation, sensor fusion with a current monitor and a search coil is used. PI controllers are used for the flux feedback control, as well as for current feedback control of the benchmarking current-controlled mode. During scanning, feedforward control is used to compensate linear dynamics. When sine motions are experimentally tested at 60-300 Hz, the current-controlled mode exhibits a nonlinearity between 6 % and 23 %, which is decreased to less than 5 % by the flux-controlled mode. For a $\pm$75 μm triangular motion at 100 Hz, the flux-controlled mode decreases the tracking error by a factor of 19 to 3.2 μm, successfully demonstrating its high-quality linear scanning motion.**

***Index Terms*—Actuators, Nanopositioning, Magnetic variables control, Motion control.**

I. Introduction

High-precision actuators are used in many motion systems. For example, micro/nanopositioners are installed in manufacturing and imaging systems, such as 3-D printers [1], atomic force microscopes [2], and optical profilers [3]. Another example is fast steering mirrors, which are utilized to scan optical beams for free-space optical communication [4] and 3-D imaging [5]. For compact size with a relatively large motion range (more than tens of micrometers and a few milliradians [6]), Lorentz actuators are typically selected and guided by flexures in these high-precision motion systems.

Lorentz actuators, including voice coil actuators, use the Lorentz force [7], which is bidirectional unlike the electrostatic force [8] and the reluctance force [9]. Lorentz actuators are highly linear for the proportionality between the input coil current and the resulting force [10], which is independent of the mover position within a uniform flux density (i.e. zero-stiffness property [7]). Such characteristics are ideal to generate linear motion in comparison with other actuators (e.g. piezoelectric actuators with hysteresis [11]). Additionally, when Lorentz actuators are guided by flexures for compactness, their closed-loop control bandwidth is significantly higher than the suspension mode's eigenfrequency by design [12]. This enables a large actuation range [13] and good vibration rejection [12]. As a result, flexure-guided Lorentz actuators realize even nanometer positioning resolution in vibrational environments [14]. However, Lorentz actuators have a relatively small motor constant (i.e. force-to-current ratio) [7] and need a large coil current and cooling mechanism to generate a high force, wasting energy in the form of heat [10], [15]. Thus, for better energy efficiency, actuators with a high motor constant and high linearity are desired in high-precision systems.

Hybrid reluctance actuators (HRAs) have a high potential for the desired performance. They use both coils and permanent magnets to create flux in ferromagnetic yokes [16]. HRAs generate a bidirectional force that is relatively proportional to the coil current and are usually regulated in the current-controlled mode [16], [17]. The motor constant of HRAs can be higher than comparable Lorentz actuators [7], and HRAs are utilized in fast steering mirrors [16], [18], fast tool servos [19], and nanopositioners [17]. However, HRAs create position-dependent force (i.e. no zero-stiffness property). It is regarded as a negative stiffness, and guiding mechanisms such as flexures with a sufficient stiffness are required for open-loop stability [17]. More critically, these actuators exhibit nonlinearities such as hysteresis and eddy currents [20], [21], in addition to the variation of the negative stiffness [17]. Such nonlinearities can be compensated by motion control (e.g. position feedback control, repetitive control, and learning control [17], [22]). However, the nonlinearities deform the scanning trajectories, resulting in a tracking error at high frequencies [23]. Consequently, the motion control's bandwidth needs to be significantly higher than the frequency components of the motion reference. This is problematic particularly for high-frequency scanning motions because the achievable bandwidth can be limited by mechanical internal modes. Furthermore, when a position sensor is used for the motion control, the positioning resolution is degraded by feeding its noise back to the actuator at high frequencies.

For highly linear scanning motion of a HRA without the above problems, this paper proposes a new operating mode for

Manuscript received June 10, 2019; revised October 18, 2019; accepted October 23, 2019. The financial support by the Christian Doppler Research Association, the Austrian Federal Ministry for Digital and Economic Affairs, the National Foundation for Research, Technology and Development, MICRO-EPSILON MESSTECHNIK GmbH & Co. KG and ATENSOR Engineering, and Technology Systems GmbH is gratefully acknowledged.

S. Ito, F. Cigarini, and G. Schitter are with Christian Doppler Laboratory for Precision Engineering for Automated In-Line Metrology, Automation and Control Institute (ACIN), TU Wien, Vienna A-1040, Austria (e-mail: ito@acin.tuwien.ac.at).

This article has been accepted for publication in a future issue of this journal, but has not been fully edited. Content may change prior to final publication. Citation information: DOI 10.1109/TIE.2019.2952829, IEEE Transactions on Industrial Electronics

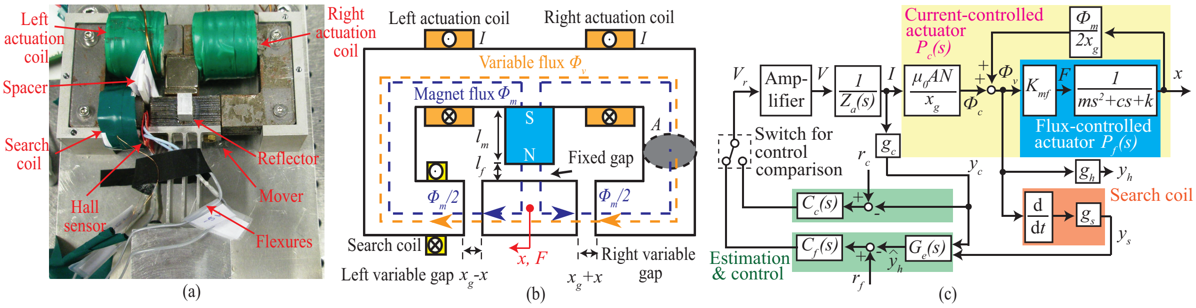

Fig. 1. Hybrid reluctance actuator (HRA): (a) photograph, (b) illustration with flux paths, (c) control block diagram with a switch to compare the proposed flux-controlled mode and the conventional current-controlled mode. The Hall sensor is removed and its output y_h is unavailable during scanning for the motion range.

HRAs: the flux-controlled mode, where controlled magnetic flux is used as the control input of a HRA. The model-based analysis in this paper reveals that the magnetic nonlinearities and the position-dependent flux are included in the variable flux selected as the control input. Consequently, they can be compensated by a flux feedback controller without a position sensor. For the feedback control, the variable flux is estimated at high resolution by utilizing sensor fusion with a search coil. The proposed flux-controlled mode is intended to replace the conventional current-controlled mode. To analyze the effectiveness of the flux-controlled mode clearly, it is experimentally compared with the current-controlled mode, without any other remedy to handle the actuator nonlinearities. The results demonstrate that even a simple PI controller significantly improves the linearity of the mover motion and stabilizes the HRA by compensating for the position-dependent force.

Flux measurement, estimation, and control have been themselves utilized for electromagnetic actuators [24]–[26]. In the case of reluctance actuators, their force is proportional to the squared flux, and this nonlinearity complicates the analysis and motion control design, or a biasing current is required, impairing the energy efficiency [7], [27], [28]. In contrast, this paper reveals that the proposed flux-controlled HRA generates a force proportional to the variable flux without a biasing current, which is desired for highly precise and accurate motion with high energy efficiency.

This paper is organized as follows. Section II introduces the proposed flux-controlled HRA. It is modeled in comparison with the conventional current-controlled mode in Section III. Section IV presents flux estimation for flux feedback control in Section V, which also discusses current feedback for comparison. The flux and current reference signals are designed to generate scanning motions in Section VI for experiments in Section VII. Section VIII concludes the paper.

II. Hardware Architecture

Figure 1(a) and (b) show the employed HRA. The stator consists of a ferromagnetic yoke with two identical actuation coils and a Nd-Fe-B permanent magnet. The ferromagnetic mover is guided by leaf-spring aluminum flexures. The ferromagnetic stator and mover are made of laminated electrical steel sheets (EN10025-S235JR) to reduce eddy current losses for energy efficiency. The mover carries a cube-corner retroreflector (43-305, Edmund optics, Barrington, USA) for measuring its position with an interferometer with a resolution of 1.25 nm/bit (10899A, Agilent Technologies, Santa Clara, USA).

The actuation coils are connected in series and used with a custom-made voltage amplifier that includes a current monitor with a shunt resistor to measure the coil current. Additionally, a search coil [29] used with a preamplifier is attached to the stator for flux estimation. The current monitor and the preamplifier are connected via 16-bit ADCs (DS2004, dSPACE, Paderborn, Germany) to a rapid prototyping system (DS1005, dSPACE) to implement the flux estimator and controllers at a sampling frequency of 60 kHz. The voltage amplifier and the interferometer are also connected to the rapid prototyping control system via a 16-bit DAC (DS2102, dSPACE) and an FPGA (DS5203, dSPACE), respectively. Fig. 1(a) additionally shows a Hall sensor (CYTHS124, ChenYang, Finsing, Germany) with a spacer in the left variable gap. Since the sensor in the gap interferes with the mover and limits the motion range, it cannot be used for real-time control, but for system identification and calibration of the flux estimator. During scanning, the Hall sensor and spacer are removed.

III. Modeling

The HRA utilizes unbalanced flux for actuation. To derive the flux for modeling, it is assumed that the yokes' permeability is sufficiently large. The magnetic reluctances of the left variable gap R_l, the right variable gap R_r, the fixed gap R_f, and the permanent magnet R_m shown in Fig. 1(b) are

$$R_l = \frac{x_g - x}{\mu_0 A},\ R_r = \frac{x_g + x}{\mu_0 A},\ R_f = \frac{l_f}{\mu_0 A},\ R_m = \frac{l_m}{\mu_0 A_m}, \tag{1}$$

where μ_0 and A are the vacuum permeability and the cross section area of the flux paths, respectively, and A_m denotes the magnet's cross section area. The left and right variable gaps are denoted by x_g when the mover is at the center, which the mover position x is measured from. The length of the fixed gap and the permanent magnet is denoted by l_f and l_m, respectively. Table I lists the nominal design parameters.

This article has been accepted for publication in a future issue of this journal, but has not been fully edited. Content may change prior to final publication. Citation information: DOI 10.1109/TIE.2019.2952829, IEEE Transactions on Industrial Electronics

TABLE I
NOMINAL DESIGN PARAMETERS

Parameter	Value	Parameter	Value
x_g	1 mm	l_f	1 mm
l_m	19 mm	A, A_m	15 mm × 15 mm
N	120	H_c	1 MA/m
k	87 kN/m	m	55 g

Because the magnet is regarded as a large air gap in (1), the flux generated by the actuation coils' current I does not go through the magnet and is given by

$$\Phi_c = 2NI/(R_l + R_r) = \mu_0 ANI/x_g, \tag{2}$$

where N is the number of windings of each actuation coil. Since l_m is way larger than l_f and x_g, the flux given by the magnet is approximated as

$$\Phi_m = \frac{H_c l_m}{R_m + R_f + \frac{R_r R_l}{R_r + R_l}} \approx \frac{H_c l_m}{R_m}, \tag{3}$$

where H_c is the coercive force of the magnet. By superimposing Φ_c and Φ_m, the flux through the left variable gap Φ_l and the right variable gap Φ_r are given by

$$\Phi_l = \Phi_c + \Phi_m R_r/(R_l + R_r) = \Phi_v + \Phi_m/2, \tag{4}$$

$$\Phi_r = \Phi_c - \Phi_m R_l/(R_l + R_r) = \Phi_v - \Phi_m/2, \tag{5}$$

where Φ_v is the variable flux defined by

$$\Phi_v = \Phi_c + \Phi_m x/(2x_g). \tag{6}$$

As illustrated in Fig. 1(b), Φ_l and Φ_r consist of the constant flux $\Phi_m/2$ and the variable flux Φ_v, which depends on x and I.

A. Flux-controlled HRA

Eq. (4) and (5) indicate that the flux in the left variable gap and in the right variable gap is unbalanced by Φ_v, resulting in the actuation force F. In the flux-controlled mode, the control input is flux, and F is written as a function of Φ_v by using the Maxwell stress tensor [21] as follows

$$F = \frac{(\Phi_v + \Phi_m/2)^2 - (\Phi_v - \Phi_m/2)^2}{2\mu_0 A} = K_{mf}\Phi_v, \tag{7}$$

where $K_{mf} = \Phi_m/(\mu_0 A)$ is the motor constant of the flux-controlled HRA. Unlike conventional modeling [30], Eq. (7) clearly indicates the proportionality between F and Φ_v. This is an important property of the proposed flux-controlled HRA for bidirectional force and linearity, in contrast to reluctance actuators, the force of which is proportional to squared flux.

Since the mover is guided by the flexures, it is modeled by a damped-mass spring system [17], resulting in the equation of motion

$$F = K_{mf}\Phi_v = m\ddot{x} + c\dot{x} + kx, \tag{8}$$

with the mover mass m and the damping c and stiffness k of the flexures. Its Laplace transform gives a transfer function from Φ_v to x

$$P_f(s) = \frac{x(s)}{\Phi_v(s)} = \frac{K_{mf}}{ms^2 + cs + k}. \tag{9}$$

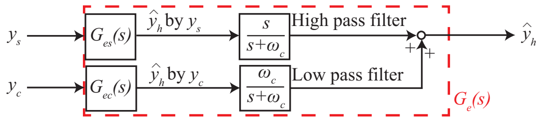

Fig. 2. Block diagram of the flux estimator $G_e(s)$ using sensor fusion.

B. Comparison with current-controlled mode

For comparison with the current-controlled mode, (7) is rewritten as a function of I by using (2)-(6) as follows [16], [19]

$$F = K_{mc} I + k_a x, \tag{10}$$

where K_{mc} and k_a are the motor constant and the actuator stiffness of the current-controlled HRA. The equation of motion of the lumped mass model with (10) gives the transfer function [17]

$$P_c(s) = \frac{x(s)}{I(s)} = \frac{K_{mc}}{ms^2 + cs + k - k_a}. \tag{11}$$

Fig. 1(c) visualizes the derived models. The problem in the current-controlled mode is that the nonlinear dynamics due to the B-H hysteresis and the residual eddy currents [21] occur between I and Φ_c. They cannot be compensated by the current feedback controller $C_c(s)$ since they are outside of the current control loop. As a result, K_{mc} in (11) varies in reality, making the current-controlled actuator nonlinear. Furthermore, current control cannot compensate for the position-dependent force $k_a x$ in (10), and this out-of-control force cancels k in (11). When the mover is far away from the center, k_a increases due to the flux leakage [31] and the magnet's flux that are influenced by x [16]. In the extreme case of $k_a > k$, an unstable pole occurs in (11), and the actuator is unstable [17]. In contrast, the control input Φ_v of the proposed flux-controlled mode includes the nonlinearities and the position-dependent flux in (6). Consequently, they are compensated by monitoring and controlling Φ_v, as discussed in the following sections. Note that the switch in Fig. 1(c) is only for the comparison of the two modes and is not toggled during the scanning operation.

IV. FLUX ESTIMATOR

A. Estimator model

For system identification, the Hall sensor is temporary installed to measure the flux $(\Phi_v + \Phi_m/2)$ in the left variable gap. Since $\Phi_m/2$ is ideally invariant, by removing the DC offset (zeroing the sensor), its output y_h approximates $g_h\Phi_v$, where the sensor gain g_h is 2.5 V/T. Since the sensor in the gap reduces the motion range, the Hall sensor is removed, and y_h is estimated by a flux estimator $G_e(s)$ based on the search coil and the current monitor during real-time control for high-quality motion (Fig. 1(c)). In this section, $G_e(s)$ is designed, as shown in Fig. 2.

The output y_s of the search coil used with its preamplifier is given by Lenz's law [29], and it is $y_s = g_s\dot{\Phi}_v$, where g_s is a gain determined by the preamplifier gain and the number of the search coil's windings that is 16. From the Laplace

This article has been accepted for publication in a future issue of this journal, but has not been fully edited. Content may change prior to final publication. Citation information: DOI 10.1109/TIE.2019.2952829, IEEE Transactions on Industrial Electronics

transform of y_s, an estimator $G_{es}(s)$ to estimate y_h from y_s is given by

$$G_{es}(s) = \frac{\hat{y}_h(s)}{y_s(s)} = \frac{g_h}{g_s s} = \frac{g_{es}}{s}, \tag{12}$$

where g_{es} is an estimator gain. While the above integrator filters the high-frequency measurement noise for precise estimation, its high gain degrades the signal-to-noise ratio at low frequencies. Furthermore, $G_{es}(s)$ is not bounded-input bounded-output (BIBO) stable, and its output signal drifts (Fig. 4(b)). As a solution, sensor fusion is used with the current monitor for flux estimation at frequencies lower than the scanning frequency. If x is sufficiently small in that frequency domain, Φ_c approximates Φ_v in (6), and an estimator is given from (2) for the current monitor output y_c by

$$G_{ec}(s) = \frac{\hat{y}_h(s)}{y_c(s)} \approx \frac{g_h \hat{\Phi}_c(s)}{y_c(s)} = \frac{g_h \mu_0 AN}{x_g g_c} = g_{ec}, \tag{13}$$

where g_c and g_{ec} are the current monitor gain (1 V/A) and an estimator gain, respectively. The current-based flux estimator cannot capture the magnetic nonlinearities but is BIBO stable.

For the sensor fusion of $G_{es}(s)$ and $G_{ec}(s)$, a complementary filter that consists of first-order low-pass and high-pass filters [25], [31] is used (Fig. 2), and the flux estimator is given from (12) and (13) by a dual-input single-output transfer function $G_e(s)$:

$$\hat{y}_h(s) = \frac{g_{ec}\omega_c}{s+\omega_c} y_c(s) + \frac{g_{es}}{s+\omega_c} y_s(s). \tag{14}$$

where ω_c is the cut-off frequency to be determined. Notice that the above filtering is BIBO stable.

B. Parameter determination

To correctly identify g_{ec} and g_{es} in (12)-(14), frequency response functions (FRFs) are measured from the voltage reference V_r to y_c, y_s, and y_h, individually. The results are used to plot $G_{es}(j\omega)$ and $G_{ec}(j\omega)$ by calculating

$$G_{es}(j\omega) = \frac{y_h(j\omega)}{V_r(j\omega)} \Bigg/ \frac{y_s(j\omega)}{V_r(j\omega)}, G_{ec}(j\omega) = \frac{y_h(j\omega)}{V_r(j\omega)} \Bigg/ \frac{y_c(j\omega)}{V_r(j\omega)} \tag{15}$$

as shown in Fig. 3. By tuning g_{es} and g_{ec}, the transfer function $G_{es}(s)$ and $G_{ec}(s)$ are fit to the measured FRFs. The results with g_{es} = 27.4 dB and g_{ec} = -13.9 dB are also shown in Fig. 3. It is visible that $G_{es}(s)$ and $G_{ec}(s)$ capture their FRFs at least up to 1 kHz and 20 Hz, respectively. The mismatch at frequencies higher than a few kilohertz may be due to the parasitic dynamics of the actuation coils [32].

Fig. 4(a) shows the power spectral density (PSD) of the flux $\hat{y}_h(s)$ estimated by the measured y_c and $G_{ec}(s)$ and by the measured y_s and $G_{es}(s)$ when V_r is set to zero. For a fair comparison, the PSD is scaled to $\mathrm{mT}/\sqrt{\mathrm{Hz}}$. The noise of the flux estimated by $G_{es}(s)$ and y_s is higher than that by $G_{ec}(s)$ and y_c below 10 Hz. To filter the low-frequency noise of y_s, ω_c is set to 10 Hz. Fig. 4(a) also shows the measured PSD of the resulting estimator $G_e(s)$ in (14). It validates that the estimator noise is successfully reduced to the level of $G_{ec}(s)$ below 10 Hz. The effectiveness is significant in the time domain, as shown in Fig. 4(b), where $\hat{y}_h$ estimated by

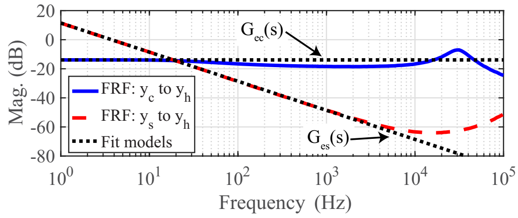

Fig. 3. Frequency response of the flux estimator $G_{es}(s)$ and $G_{ec}(s)$ that are fit to the corresponding FRFs given by (15) based on experiments.

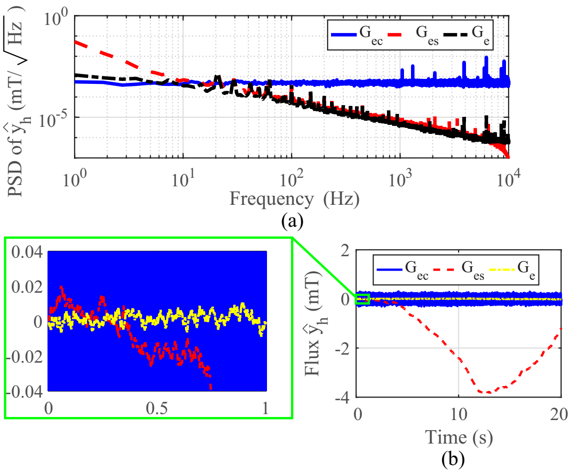

Fig. 4. Experimental results showing flux estimated by $G_{es}(s)$ with the search coil, $G_{ec}(s)$ with the current monitor, and $G_e(s)$ for sensor fusion: (a) PSD and (b) time-domain signals.

$G_e(s)$ shows less noise of 8.7 $\mu\mathrm{T_{rms}}$ than that by $G_{ec}(s)$ (57 $\mu\mathrm{T_{rms}}$) without drift. Additionally, measured Bode plots from V_r to y_h and to $\hat{y}_h$ estimated by $G_e(s)$ are compared in Fig. 5, which clearly shows that $G_e(s)$ is capable of estimating y_h up to about 3 kHz. Note that the dynamics in Fig. 5 have low-pass characteristics due to the impedance of the actuation coils denoted by $Z_a(s)$ in Fig. 1(c).

V. Feedback Control for Flux- and Current-Controlled Modes

Since the flux estimation error increases above 3 kHz in Fig. 5, a flux feedback controller $C_f(s)$ (see Fig. 1(c)) for the flux-controlled mode is designed for an open-loop cross-over frequency of 3 kHz with a sufficient phase margin (PM) of 55 deg. For this purpose, a PI controller is implemented by

$$C_f(s) = k_{pf} + k_{pf}\omega_{cf}/s. \tag{16}$$

The P gain k_{pf} and the corner frequency ω_{cf} are set to 50.8 dB and 300 Hz to satisfy the requirements by using a simulated open-loop transfer function based on the measured response from V_r to $\hat{y}_h$ in Fig. 5. Fig. 6(a) shows the simulated plot, indicating that the requirements are satisfied.

Similarly, another PI controller $C_c(s)$ (see Fig. 1(c)) is designed for the current-controlled mode. The red dashed line

Post-print version of the article: S. Ito, F. Cigarini, and G. Schitter, " Flux-controlled Hybrid Reluctance Actuator for High-precision Scanning Motion," *IEEE Transactions on Industrial Electronics*, 2019. DOI: 10.1109/TIE.2019.2952829

This article has been accepted for publication in a future issue of this journal, but has not been fully edited. Content may change prior to final publication. Citation information: DOI 10.1109/TIE.2019.2952829, IEEE Transactions on Industrial Electronics

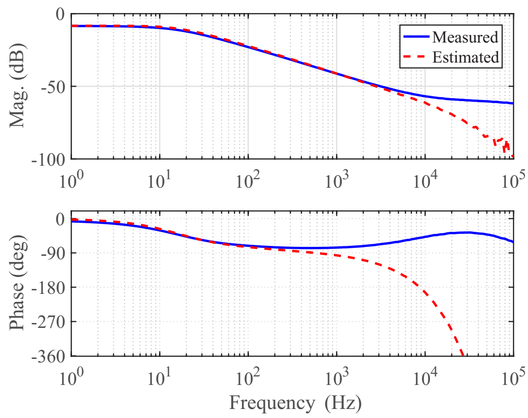

Fig. 5. Bode plots from V_r to y_h measured by the Hall sensor and estimated by the implemented $G_e(s)$ for validation.

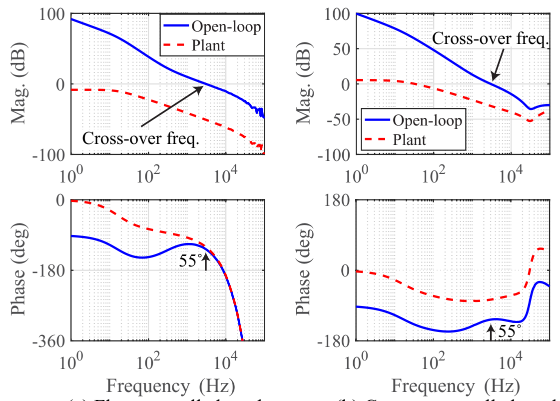

(a) Flux-controlled mode (b) Current-controlled mode

Fig. 6. Simulated open-loop transfer function: (a) for flux feedback control design with the measured Bode plot from V_r to $\hat{y}_h$ as the plant and (b) for current feedback control design with the measured Bode plot from V_r to y_c as the plant. The arrows indicate the open-loop cross-over frequency and the phase margin.

in Fig. 6(right) shows a Bode plot from V_r to y_c as the plant. Notice that the gain increases at high frequencies due to the parasitic dynamics. To decrease the open-loop gain at high frequencies for stability, a low-pass filter is included in $C_c(s)$ as follows

$$C_c(s) = \frac{1}{s/(\alpha_c\omega_{cc})+1}\left(k_{pc} + \frac{k_{pc}\omega_{cc}}{\alpha_c s}\right), \tag{17}$$

where k_{pc}, ω_{cc} and α_c are the P gain, the desired cross-over frequency, and a parameter to tune PM, respectively. For a fair comparison with the flux control, k_{pc}, ω_{cc} and α_c are tuned to 31.2 dB, 3 kHz, and 2.1, respectively, such that the open-loop cross-over frequency and PM are also 3 kHz and 55 deg, as shown in Fig. 6(b).

For evaluation, the complementary sensitivity functions from r_c to y_c and from r_f to $\hat{y}_h$ (see Fig. 1(c)) are measured as shown in Fig. 7(a). The current-controlled and flux-controlled modes show similar behavior as desired, with a (-3 dB)

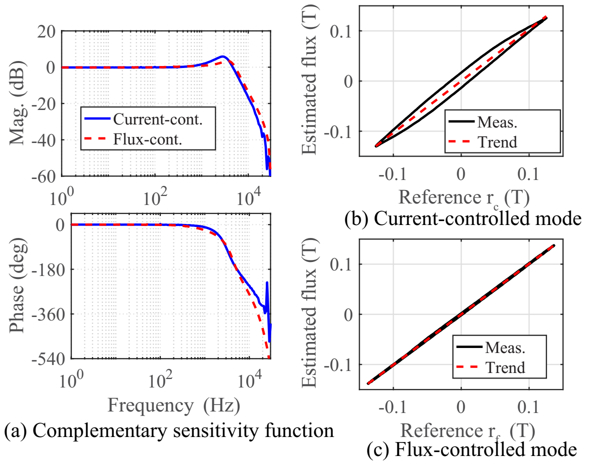

(a) Complementary sensitivity function (b) Current-controlled mode (c) Flux-controlled mode

Fig. 7. Experimental closed-loop validation: (a) complementary sensitivity function, and (b)(c) hysteresis loops evaluated by $\hat{y}_h$ estimated by the implemented $G_e(s)$ with 100 Hz sine inputs in the current-controlled mode and the flux-controlled mode.

bandwidth of 5.4 kHz and 6.0 kHz, respectively. Additionally, 100 Hz sinusoidal references are used to evaluate Lissajous curves. Fig. 7(b) demonstrates that the flux estimator $G_e(s)$ captures the hysteresis of the current-controlled mode. It is compensated by the flux-controlled mode in Fig. 7(c). When the trend lines in Fig. 7(b)(c) are used to calculate nonlinearity (mapping errors divided by scan ranges [33]), the nonlinearity due to the hysteresis is 6.8 % and 1.1 % for the current-controlled and flux-controlled modes, respectively.

VI. Motion Control

A. Trajectory

To evaluate scanning motions, sine waves are used, as well as a band-limited triangular wave, which is commonly used for imaging systems (e.g. [14]). These waves are periodic and given in the form of Fourier series

$$r_x(t) = \sum_{k=1}^{l}(c_k e^{jk\omega_x t} + c_k^* e^{-jk\omega_x t}), \tag{18}$$

where t, l, c_k, and c_k^* are the time, the highest harmonic, the complex Fourier coefficient of the k-th harmonic, and its conjugate, respectively. As discussed in Section IV-A, the scanning frequency ω_x needs to be sufficiently higher than $\omega_c = 10$ Hz of the flux estimator $G_e(s)$, where the current-based flux estimation dominates without capturing the nonlinearities. Note that (18) has no DC component for the scanning motion evaluation. For sine waves with an amplitude of A_x, $r_x(t)$ consists of $c_1 = -jA_x/2$ and c_1^* only. In the case of the triangular wave, the coefficients are given by

$$c_k = -j\frac{4A_x}{\pi^2 k^2}\sin\left(\frac{k\pi}{2}\right). \tag{19}$$

For the triangular scanning at 100 Hz, A_x and l are set to 75 μm and 7, respectively.

This article has been accepted for publication in a future issue of this journal, but has not been fully edited. Content may change prior to final publication. Citation information: DOI 10.1109/TIE.2019.2952829, IEEE Transactions on Industrial Electronics

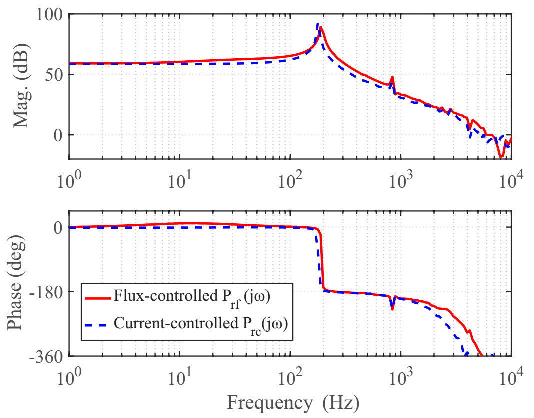

Fig. 8. Measured FRF $P_{rf}(j\omega)$ from r_f to x and $P_{rc}(j\omega)$ from r_c to x, where the gain is scaled to μm/T for a better comparison.

B. Linear feedforward control

The HRA exhibits nonlinear as well as linear dynamics. In order to investigate them, after the spacer and the Hall sensor are removed, Bode plots are measured from the flux reference r_f to x for the flux-controlled mode and from the current reference r_c to x for the current-controlled mode, respectively. They are denoted by $P_{rf}(j\omega)$ and $P_{rc}(j\omega)$ and shown in Fig.8, where the suspension mode predicted by (9) and (11) is visible around 200 Hz together with mechanical internal modes (>800 Hz) and phase lag due to the sampling. They are compensated by Fourier-based linear feedforward control [34] to generate r_f and r_c as follows

$$r_f(t) = \sum_{k=1}^{l} \left(\frac{c_k e^{jk\omega_x t}}{P_{rf}(jk\omega_x)} + \frac{c_k^* e^{-jk\omega_x t}}{P_{rf}^*(jk\omega_x)} \right), \tag{20}$$

$$r_c(t) = \sum_{k=1}^{l} \left(\frac{c_k e^{jk\omega_x t}}{P_{rc}(jk\omega_x)} + \frac{c_k^* e^{-jk\omega_x t}}{P_{rc}^*(jk\omega_x)} \right). \tag{21}$$

In the above equations, the amplitude is corrected independently of the phase and vice versa at each frequency. This enables to compensate for non-minimum phase zeros, unlike feedforward control using the inverse of a transfer function model, which turns non-minimum phase zeros into unstable poles [35].

VII. Experiments

In this section, the proposed flux-controlled mode is evaluated in comparison with the conventional current-controlled mode.

A. Linearity

When a sine wave is used as the reference r_x, the mover position x and the tracking error $e_x = r_x - x$ are measured. From the measured x, the nonlinearity is calculated with a linear trend line by dividing the mapping errors by the scan range [33]. As shown in Fig. 9(a)(b), when the current-controlled mode is used, the nonlinearity varies between 6 % and 23 %, dependent on the scanning frequency ω_x and the amplitude A_x. The large nonlinearity is decreased to less than 5 % by using the flux-controlled mode. Particularly at $\omega_x = 60$ Hz and $A_x = 30\,\mu$m (Fig. 9(b)), the current-controlled mode shows large nonlinearity of 23 %. This is because the actuator nonlinearities deform the mover motion, and the resulting third harmonic excites the suspension mode at 180 Hz (Fig. 8) [30]. In contrast, the flux-controlled mode achieves 4.7 % nonlinearity, which is smaller by a factor of 4.8. Even if ω_x is increased to 65 Hz, which is about one third of the flux-controlled actuator's resonance (193 Hz), the nonlinearity is 4.7 % only, demonstrating the improved linear motion.

It is clear that the tracking error improvement by the flux-controlled mode is more significant for the 30 μm trajectory than for the 1 μm. To analyze this amplitude dependency, the normalized error in rms e_x/A_x is measured for $\omega_x = 100$ Hz when A_x is increased from 1 μm to 200 μm. Fig. 9(c) shows that the current-controlled mode significantly increases the normalized error as A_x increases. Particularly for $A_x = 200\,\mu$m, the mover collides with the stator. Such phenomena can be explained by the actuator stiffness k_a of the current-controlled HRA in (10). When the mover goes away from the origin, k_a increases and changes the plant model (11) [17], resulting in a mismatch with P_{rc} of the feedforward control (21) and in a larger tracking error. Eventually, the actuator can be unstable due to the uncontrollable positive flux feedback loop in Fig. 1(c).

As discussed in Section III, the problematic position-dependent flux is regarded as a disturbance in the case of the flux-controlled mode and can be rejected by the flux feedback controller. The experiments in Fig. 9(c) verify the model-based analysis. In the the flux-controlled mode, the normalized error is less than 8.3 % over the entire amplitude range, and the stable actuator operation is realized even for $A_x = 200\,\mu$m.

B. Triangular scanning motion

The linear sine motions of the flux-controlled actuator in Section VII-A imply its capability to realize an arbitrary periodic scanning motion by superimposing them. This capability is demonstrated by using the triangular trajectory designed in Section VI-A. Fig. 10(a)(b) shows that the current-controlled mode generates a significantly larger motion than the desired motion of $\pm 75\,\mu$m. The tracking error e_x changes between -116 μm and 93 μm, resulting in an rms value of 60 μm. The flux-controlled mode decreases this large rms error by a factor of 19 to 3.2 μm.

More importantly, the spectrum of the tracking error in Fig. 10(c) shows that the current-controlled mode's e_x has frequency components up to about 2 kHz, which is far higher than the highest harmonic frequency 700 Hz of the reference r_x. This is because the nonlinearities deform the scanning motion and create the higher harmonics. They are unwanted as they may excite mechanical internal modes. In contrast, the error spectrum in the flux-controlled mode is up to 800 Hz and stays at the noise floor level at higher frequencies, due to its high linearity. This property is more important when the scanning motion is further improved by combining motion

This article has been accepted for publication in a future issue of this journal, but has not been fully edited. Content may change prior to final publication. Citation information: DOI 10.1109/TIE.2019.2952829, IEEE Transactions on Industrial Electronics

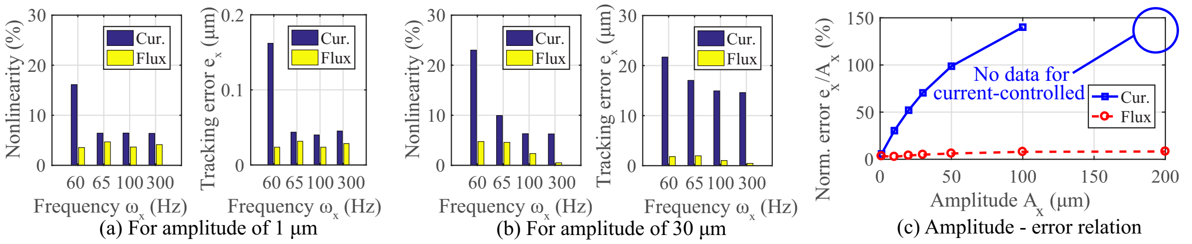

Fig. 9. Measured nonlinearity of x and tracking error $e_x = r_x - x$ in rms, comparing the flux-controlled and current-controlled modes, for sine motions with an amplitude A_x of (a) 1 μm and (b) 30 μm. The plot (c) shows the relation between A_x and the normalized error in rms e_x/A_x for the scanning frequency ω_x of 100 Hz. The tracking error for $A_x = 200\,\mu$m cannot be measured in the current-controlled mode because of a mover collision with the stator.

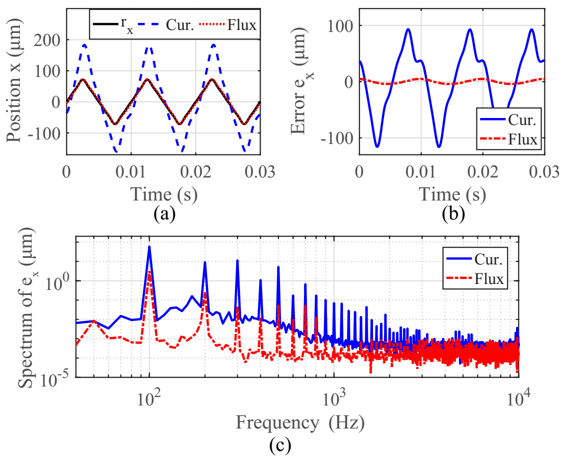

Fig. 10. Measured 100 Hz triangular motions in the flux-controlled mode and in the current-controlled modes: (a) measured position x, (b) tracking error e_x, and (c) the spectrum of e_x.

control with a position sensor (e.g. position feedback control, repetitive control, and learning control [17], [22]). For the compensation of the residual tracking error, the motion control needs to have a bandwidth of 2 kHz in the current-controlled mode, which is significantly decreased to 800 Hz in the flux-controlled mode. This relaxed requirement in the flux-controlled mode is beneficial for high-precision motion, reducing the measurement noise that is fed back to the HRA by the motion control.

In summary, the proposed flux-controlled HRA realizes more stable operation, higher linearity, and smaller tracking error by regulating the variable flux, in comparison with the conventional current-controlled mode.

VIII. Conclusion

This paper proposes a flux-controlled HRA by using its variable flux as the control input. A model-based analysis reveals that the position-dependent flux and the magnetic nonlinearities are included in the control input. To capture them, sensor fusion is used with a current monitor and a search coil to precisely and accurately estimate the variable flux without drift in a targeted scanning frequency band. The captured nonlinearities are rejected by flux feedback control, which is implemented by a PI controller. For the benchmarking current-controlled mode, a low-pass-filtered PI controller is designed for fair comparison. Furthermore, the reference signals are individually designed to compensate for the linear dynamics. The experiments demonstrate that the nonlinearity of sine scanning motions is up to 23 % in the current-controlled mode while it is less than 5 % in the flux-controlled mode. When the $\pm 75\,\mu$m triangular reference is used for 100 Hz scanning, the current-controlled mode results in the large distorted tracking error of 60 μm. The flux-controlled mode decreases it to 3.2 μm, demonstrating its improved linearity achieved by the regulated flux control input. Future work includes accurate flux estimation at low frequencies, in order to expand the applications of the highly linear HRAs in the flux-controlled mode.

Acknowledgment

The authors would like to thank Mr. Julian Konig for electronics development and fruitful discussions.

References

[1] J. Stampfl, R. Liska, and A. Ovsianikov, *Multiphoton Lithography: Techniques, Materials and Applications*. Wiley-VCH, 2016.
[2] M. Loganathan, A. Al-Ogaidi, and D. A. Bristow, "Design and control of a dual-probe atomic force microscope," *IEEE/ASME Transactions on Mechatronics*, vol. 23, DOI 10.1109/TMECH.2017.2779241, no. 1, pp. 424–433, 2018.
[3] M. Hillenbrand, R. Weiss, C. Endrödy, A. Grewe, M. Hoffmann, and S. Sinzinger, "Chromatic confocal matrix sensor with actuated pinhole arrays," *Appl. Opt.*, vol. 54, DOI 10.1364/AO.54.004927, no. 15, pp. 4927–4936, 2015.
[4] W. S. Rabinovich, C. I. Moore, R. Mahon, P. G. Goetz, H. R. Burris, M. S. Ferraro, J. L. Murphy, L. M. Thomas, G. C. Gilbreath, M. Vilcheck, and M. R. Suite, "Free-space optical communications research and demonstrations at the u.s. naval research laboratory," *Appl. Opt.*, vol. 54, DOI 10.1364/AO.54.00F189, no. 31, pp. F189–F200, 2015.
[5] J. Schlarp, E. Csencsics, and G. Schitter, "Optical scanning of laser line sensors for 3d imaging," *Appl. Opt.*, vol. 57, DOI 10.1364/AO.57.005242, no. 18, pp. 5242–5248, 2018.
[6] E. Csencsics, "Integrated design of high performance mechatronics for optical inline metrology systems," Ph.D. dissertation, Faculty of Electrical Engineering and Information Technology, TU Wien, 2017.
[7] R. Munnig Schmidt, G. Schitter, A. Rankers, and J. van Eijk, *The Design of High Performance Mechatronics*, 2nd ed. Delft University Press, 2014.

[8] R. Schroedter, M. Roth, K. Janschek, and T. Sandner, "Flatness-based open-loop and closed-loop control for electrostatic quasi-static microscanners using jerk-limited trajectory design," *Mechatronics*, vol. 56, DOI 10.1016/j.mechatronics.2017.03.005, pp. 318–331, 2018.

[9] X. Xue, K. W. E. Cheng, and Z. Zhang, "Model, analysis, and application of tubular linear switched reluctance actuator for linear compressors," *IEEE Transactions on Industrial Electronics*, vol. 65, DOI 10.1109/TIE.2018.2818638, no. 12, pp. 9863–9872, 2018.

[10] T. Tuma, W. Haeberle, H. Rothuizen, J. Lygeros, A. Pantazi, and A. Sebastian, "Dual-stage nanopositioning for high-speed scanning probe microscopy," *IEEE/ASME Transactions on Mechatronics*, vol. 19, DOI 10.1109/TMECH.2013.2266481, no. 3, pp. 1035–1045, 2014.

[11] C. Yang, C. Li, and J. Zhao, "A nonlinear charge controller with tunable precision for highly linear operation of piezoelectric stack actuators," *IEEE Transactions on Industrial Electronics*, vol. 64, DOI 10.1109/TIE.2017.2698398, no. 11, pp. 8618–8625, 2017.

[12] S. Ito and G. Schitter, "Comparison and classification of high-precision actuators based on stiffness influencing vibration isolation," *IEEE/ASME Transactions on Mechatronics*, vol. 21, DOI 10.1109/TMECH.2015.2478658, no. 2, pp. 1169–1178, 2016.

[13] G. Parmar, K. Barton, and S. Awtar, "Large dynamic range nanopositioning using iterative learning control," *Precision Engineering*, vol. 38, DOI 10.1016/j.precisioneng.2013.07.003, no. 1, pp. 48–56, 2014.

[14] S. Ito and G. Schitter, "Atomic force microscopy capable of vibration isolation with low-stiffness z-axis actuation," *Ultramicroscopy*, vol. 186, DOI 10.1016/j.ultramic.2017.12.007, pp. 9–17, 2018.

[15] D. B. Hiemstra, G. Parmar, and S. Awtar, "Performance trade-offs posed by moving magnet actuators in flexure-based nanopositioning," *IEEE/ASME Transactions on Mechatronics*, vol. 19, DOI 10.1109/TMECH.2012.2226738, no. 1, pp. 201–212, 2014.

[16] D. J. Kluk, M. T. Boulet, and D. L. Trumper, "A high-bandwidth, high-precision, two-axis steering mirror with moving iron actuator," *Mechatronics*, vol. 22, DOI 10.1016/j.mechatronics.2012.01.008, no. 3, pp. 257–270, 2012, special Issue on Mechatronic Systems for Micro- and Nanoscale Applications.

[17] S. Ito, S. Troppmair, B. Lindner, F. Cigarini, and G. Schitter, "Long-range fast nanopositioner using nonlinearities of hybrid reluctance actuator for energy efficiency," *IEEE Transactions on Industrial Electronics*, vol. 66, DOI 10.1109/TIE.2018.2842735, no. 4, pp. 3051–3059, 2019.

[18] E. Csencsics, J. Schlarp, and G. Schitter, "High-performance hybrid-reluctance-force-based tip/tilt system: Design, control, and evaluation," *IEEE/ASME Transactions on Mechatronics*, vol. 23, DOI 10.1109/TMECH.2018.2866272, no. 5, pp. 2494–2502, 2018.

[19] D. Wu, X. Xie, and S. Zhou, "Design of a normal stress electromagnetic fast linear actuator," *IEEE Transactions on Magnetics*, vol. 46, DOI 10.1109/TMAG.2009.2036606, no. 4, pp. 1007–1014, 2010.

[20] E. Csencsics, J. Schlarp, and G. Schitter, "Bandwidth extension of hybrid-reluctance-force-based tip/tilt system by reduction of eddy currents," in *2017 IEEE International Conference on Advanced Intelligent Mechatronics (AIM)*, DOI 10.1109/AIM.2017.8014176, pp. 1167–1172, 2017.

[21] E. P. Furlani, *Permanent Magnet and Electromechanical Devices*. Academic Press, 2001.

[22] X. Lu, "Electromagnetically-driven ultra-fast tool servos for diamond turning," Ph.D. dissertation, Massachusetts Institute of Technology, 2005.

[23] S. Ito, S. Troppmair, F. Cigarini, and G. Schitter, "High-speed scanner with nanometer resolution using a hybrid reluctance force actuator," *IEEJ Journal of Industry Applications*, vol. 8, DOI 10.1541/ieejjia.8.170, no. 2, pp. 170–176, 2019.

[24] N. J. Groom, "A magnetic bearing control approach using flux feedback (nasa-tm-100672)," National Aeronautics and Space Administration, Tech. Rep., 1989.

[25] D. Amin-Shahidi, I. MacKenzie, and D. Trumper, "Magnetic flux linkage estimation and control for a reluctance actuator," in *ASPE Spring Topical Meeting*, 2013.

[28] M. A, "Lyapunov sliding-mode observers with application for active magnetic bearing operated with zero-bias flux," *Journal of Dynamic Systems, Measurement, and Control*, vol. 141, DOI 10.1115/1.4041978, no. 4, pp. 041 006–12, 2018.

[26] E. Ramirez-Laboreo, E. Moya-Lasheras, and C. Sagues, "Real-time electromagnetic estimation for reluctance actuators," *IEEE Transactions on Industrial Electronics*, vol. 66, DOI 10.1109/TIE.2018.2838077, no. 3, pp. 1952–1961, 2019.

[27] A. Katalenic, H. Butler, and P. P. J. van den Bosch, "High-precision force control of short-stroke reluctance actuators with an air gap observer," *IEEE/ASME Transactions on Mechatronics*, vol. 21, DOI 10.1109/TMECH.2016.2569023, no. 5, pp. 2431–2439, 2016.

[29] A. Roux, O. Le Contel, C. Coillot, A. Bouabdellah, B. de la Porte, D. Alison, S. Ruocco, and M. C. Vassal, "The search coil magnetometer for themis," *Space Science Reviews*, vol. 141, DOI 10.1007/s11214-008-9455-8, no. 1, pp. 265–275, 2008.

[30] F. Cigarini, S. Ito, J. Konig, A. Sinn, and G. Schitter, "Compensation of hysteresis in hybrid reluctance actuator for high-precision motion," in *IFAC Symposium on Mechatronic Systems*, 2019.

[31] F. Cigarini, S. Ito, S. Troppmair, and G. Schitter, "Comparative finite element analysis of a voice coil actuator and a hybrid reluctance actuator," *IEEJ Journal of Industry Applications*, vol. 8, DOI 10.1541/ieejjia.8.192, no. 2, pp. 192–199, 2019.

[32] A. Massarini, "Analytical approach to the calculation of parasitic capacitance between winding turns," in *IEEE International Forum on Research and Technology for Society and Industry*, DOI 10.1109/RTSI.2018.8548511, pp. 1–4, 2018.

[33] A. J. Fleming, "A review of nanometer resolution position sensors: Operation and performance," *Sensors and Actuators A: Physical*, vol. 190, DOI 10.1016/j.sna.2012.10.016, pp. 106–126, 2013.

[34] S. Ito, D. Neyer, J. Steininger, and G. Schitter, "Dual actuation of fast scanning axis for high-speed atomic force microscopy," *IFAC-PapersOnLine*, vol. 50, DOI 10.1016/j.ifacol.2017.08.1156, no. 1, pp. 7633–7638, 2017, 20th IFAC World Congress.

[35] T. Yamaguchi, M. Hirata, and C. Pang, *High-Speed Precision Motion Control*. Taylor & Francis, 2011.

Shingo Ito received the MASc in Mechanical and Industrial Engineering from the University of Toronto, Canada, in 2007 and the PhD in Electrical Engineering from TU Wien, Vienna, Austria in 2015. From 2007 to 2010, he served as an engineer in the field of motion control at Yaskawa Electric Corporation, Japan.

He is currently a postdoctoral researcher at the Automation and Control Institute (ACIN), TU Wien. His research interest includes design and control of high-precision mechatronic systems for production, inspection and automation.

Francesco Cigarini is a PhD student at the Automation and Control Institute (ACIN) of TU Wien, Vienna, Austria. He received the MSc degree in mechatronic engineering from the University of Modena and Reggio Emilia, Reggio Emilia, Italy (2012). His research interest includes the design of mechatronic systems, inline metrology systems and multiphysics FEM analysis of electro-mechanical systems.

This article has been accepted for publication in a future issue of this journal, but has not been fully edited. Content may change prior to final publication. Citation information: DOI 10.1109/TIE.2019.2952829, IEEE Transactions on Industrial Electronics

Georg Schitter (SM'11) received the M.Sc. degree in electrical engineering from TU Graz, Austria in 2000, and the M.Sc. degree in information technology and the Ph.D. degree in technical sciences from ETH Zurich, Zurich, Switzerland, in 2004.

He is currently a Professor for Advanced Mechatronic Systems with the Automation and Control Institute, TU Wien, Vienna, Austria. His research interests include high-performance mechatronic systems, particularly for applications in the high-tech industry, scientific instrumentation, and mechatronic imaging systems, such as AFM, scanning laser and LIDAR systems, telescope systems, adaptive optics, and lithography systems for semiconductor industry.

Dr. Schitter received the IFAC Mechatronics best paper award (2008-2011) and 2013 IFAC Mechatronics Young Researcher Award, and was an Associate Editor for IFAC Mechatronics, Control Engineering Practice, and IEEE-TRANSACTIONS ON MECHATRONICS.